AFRL-RV-PS-
TP-2014-0008

AFRL-RV-PS-
TP-2014-0008

ENERGY COUPLING DURING THE AUGUST 2011 MAGNETIC STORM (POSTPRINT)

C. Y. Huang, et al.

27 August 2014

Journal Article

AIR FORCE RESEARCH LABORATORY
Space Vehicles Directorate
3550 Aberdeen Ave SE
AIR FORCE MATERIEL COMMAND
KIRTLAND AIR FORCE BASE, NM 87117-5776

REPORT DOCUMENTATION PAGE

Form Approved
OMB No. 0704-0188

1. REPORT DATE *(DD-MM-YYYY)*	**2. REPORT TYPE**	**3. DATES COVERED** *(From - To)*
27-08-2014	Journal Article	27 Aug 2012 – 27 Aug 2014

4. TITLE AND SUBTITLE
Energy Coupling During the August 2011 Magnetic Storm (Postprint)

5a. CONTRACT NUMBER

5b. GRANT NUMBER

5c. PROGRAM ELEMENT NUMBER
61102F

6. AUTHOR(S)
C. Y. Huang, Y.-J. Su, E. K. Sutton, D. R. Weimer, and R. L. Davidson

5d. PROJECT NUMBER
2301

5e. TASK NUMBER
PPM00005202

5f. WORK UNIT NUMBER
EF004378

7. PERFORMING ORGANIZATION NAME(S) AND ADDRESS(ES)

Air Force Research Laboratory
Space Vehicles Directorate
3550 Aberdeen Avenue SE
Kirtland AFB, NM 87117-5776

8. PERFORMING ORGANIZATION REPORT NUMBER

AFRL-RV-PS-TP-2014-0008

9. SPONSORING / MONITORING AGENCY NAME(S) AND ADDRESS(ES)

10. SPONSOR/MONITOR'S ACRONYM(S)
AFRL/RVBXP

11. SPONSOR/MONITOR'S REPORT NUMBER(S)

12. DISTRIBUTION / AVAILABILITY STATEMENT

Approved for public release; distribution is unlimited. (377ABW-2013-0558 dtd 01 Jul 2013)

13. SUPPLEMENTARY NOTES
Accepted for publication in Journal of Geophysical Research: Space Physics: 16 Jan 2014. Government Purpose Rights

14. ABSTRACT

We present results from an analysis of high-latitude ionosphere-thermosphere (IT) coupling to the solar wind during a moderate magnetic storm which occurred on 5–6 August 2011. During the storm, a multipoint set of observations of the ionosphere and thermosphere was available. We make use of ionospheric measurements of electromagnetic and particle energy made by the Defense Meteorological Satellite Program and neutral densities measured by the Gravity Recovery and Climate Experiment satellite to infer (1) the energy budget and (2) timing of the energy transfer process during the storm. We conclude that the primary location for energy input to the IT system may be the extremely high latitude region. We suggest that the total energy available to the IT system is not completely captured either by observation or empirical models.

15. SUBJECT TERMS
Thermosphere, polar cap, magnetic storm

16. SECURITY CLASSIFICATION OF:			**17. LIMITATION OF ABSTRACT**	**18. NUMBER OF PAGES**	**19a. NAME OF RESPONSIBLE PERSON**
a. REPORT	**b. ABSTRACT**	**c. THIS PAGE**			Dr. Cheryl Huang
Unclassified	Unclassified	Unclassified	Unlimited	18	**19b. TELEPHONE NUMBER** *(include area code)*

AGU PUBLICATIONS

JGR

Journal of Geophysical Research: Space Physics

RESEARCH ARTICLE
10.1002/2013JA019297

Key Points:
- Thermosphere is major sink for storm energy
- Thermosphere energized in polar cap
- Models do not capture polar cap interactions

Correspondence to:
C. Y. Huang,
cheryl.huang@us.af.mil

Citation:
Huang, C. Y., Y.-J. Su, E. K. Sutton, D. R. Weimer, and R. L. Davidson (2014), Energy coupling during the August 2011 magnetic storm, *J. Geophys. Res. Space Physics*, *119*, 1219–1232, doi:10.1002/2013JA019297.

Received 6 AUG 2013
Accepted 16 JAN 2014
Accepted article online 17 JAN 2014
Published online 11 FEB 2014

Energy coupling during the August 2011 magnetic storm

C. Y. Huang[1], Y.-J. Su[1], E. K. Sutton[1], D. R. Weimer[2,3], and R. L. Davidson[2]

[1]Space Vehicles Directorate, Air Force Research Laboratory, Albuquerque, New Mexico, USA, [2]Center for Space Science and Engineering Research, Virginia Polytechnic Institute and State University, Blacksburg, Virginia, USA, [3]National Institute of Aerospace, Hampton, Virginia, USA

Abstract We present results from an analysis of high-latitude ionosphere-thermosphere (IT) coupling to the solar wind during a moderate magnetic storm which occurred on 5–6 August 2011. During the storm, a multipoint set of observations of the ionosphere and thermosphere was available. We make use of ionospheric measurements of electromagnetic and particle energy made by the Defense Meteorological Satellite Program and neutral densities measured by the Gravity Recovery and Climate Experiment satellite to infer (1) the energy budget and (2) timing of the energy transfer process during the storm. We conclude that the primary location for energy input to the IT system may be the extremely high latitude region. We suggest that the total energy available to the IT system is not completely captured either by observation or empirical models.

1. Introduction

Energy budgets for magnetic storms have been computed for single events as well as for large statistical studies. The major focus in previous studies has been on ionospheric processes which occur in the auroral zones and storage of energy in the ring current [*Akasofu*, 1981; *Weiss et al*., 1992; *Knipp et al*., 1998; *Li et al*., 2012, and references therein]. In this paper we include the thermosphere as a sink for storm energy and compare the amount of energy required to raise thermospheric temperatures from prestorm levels with that measured in the form of Poynting flux, particle precipitation, and increases in ring current energy. We focus on a single magnetic storm. The August 2011 storm occurred during a period when comprehensive measurements of the solar wind, ionosphere, and thermosphere were available from the Advanced Composition Explorer, Defense Meteorological Satellite Program (DMSP), Gravity Recovery and Climate Experiment (GRACE), and the Communications/Navigation Outage Forecast System (C/NOFS) spacecraft. These provide information on the energy available from the solar wind to drive ionosphere-thermosphere (IT) processes and the energies recorded in the ionosphere and thermosphere during the storm. We also use the empirical output from the High Accuracy Satellite Drag Model (HASDM) [*Casali and Barker*, 2002; *Storz et al*., 2002] for neutral densities. We combine ionospheric observations of Poynting flux and particle precipitation with the Weimer empirical models of ionospheric Joule heating and thermospheric responses [*Weimer*, 2005; *Weimer et al*., 2011] (hereafter W05) and the Hemispheric Power [*Evans*, 1987] (HP). We compare the energy available to the thermosphere with other energy sinks, and we analyze the timing of the thermospheric response during the storm. Solar wind energy input is estimated from data downloaded from the OMNIWeb site (http://omniweb.gsfc.nasa.gov/form/omni_min.html). Ground magnetic indices (*Dst* and *Sym-H*) are downloaded from World Data Center A (Kyoto) website (http://wdc.kugi.kyoto-u.ac.jp/).

Response of the thermosphere to storm activity has been studied for limited classes of storms [*Burke et al*., 2009; *Wilson et al*., 2006; *Liu et al*., 2010; *Knipp et al*., 2013]. However, in these studies, the thermospheric response is treated as an isolated entity, separate from the ionospheric responses. In general, when the energetics of stormtime budgets are considered, ionospheric sinks are limited to auroral processes, e.g., particle precipitation, auroral Joule heating or Poynting flux input, and field-aligned currents [*Li et al*., 2012]. No interactions in the open field line region poleward of the auroral zone are considered important to overall energy considerations. In this paper, we consider all these processes together with ring current energization and thermospheric heating as the total IT response to energy dissipation during storms and compare the relative magnitudes and timing of energy response of the IT system under conditions of solar wind driving. By taking this approach we arrive at the surprising conclusion that the primary location for energy input to the IT system may be the open field line region poleward of the aurora. This hypothesis is tested by direct observations of thermospheric

densities and Traveling Atmospheric Disturbances (TADs) as functions of latitude during the storm main phase. These confirm that after the onset of the magnetic storm, neutral densities initially increase at orbital extrema, i.e., in the polar cap.

2. Instrumentation

DMSP satellites are three-axis stabilized spacecraft that fly in circular, Sun-synchronous, polar (inclination 98.7°) orbits at an altitude of approximately 840 km. The geographic local times of the orbits are either near the 1800–0600 (F15, F17) or 2000–0800 (F16, F18) local time meridians. Offsets between the geographic and geomagnetic poles allow DMSP satellites to sample wide ranges of magnetic local times over the course of a day. The ascending nodes of DMSP orbits are on the duskside of the Earth. Thus, the satellites move toward the northwest in the evening sector and southeast in the morning sector. Each satellite carries sensors to measure densities, temperatures, and drift motions of ionospheric ions and electrons (Special Sensor for Ions Electrons and Scintillations (SSIES)). All of the satellites carry magnetometers (Special Sensor for Magnetic Fields (SSM)) to monitor perturbations of the Earth's magnetic field. For this study, we use F15, F16, and the Southern Hemisphere passes made by F18.

Each SSIES instrument package consists of a spherical Langmuir probe mounted on a 25 cm boom to measure the density and temperature of ambient electrons, and three different sensors mounted on a planar conducting plate facing the ram direction. These are (1) an ion trap to measure the total ion density, (2) an ion drift meter (IDM) to measure horizontal (V_H) and vertical (V_V) cross-track components of the plasma drift, and (3) a retarding potential analyzer (RPA) to measure ion temperatures and in-track components of plasma drift V_k [*Rich and Hairston*, 1994]. Shapes of RPA current-voltage sweeps can be used to determine the percentages of O^+ and light ion species (H^+ and He^+). Because of the large sensitivity of in-track velocity measurements to uncertainties in the spacecraft potential, RPA estimates of in-track velocity often have large error bars and are not used in this study. We use 1 s averages of the horizontal cross-track plasma drifts in this study.

SSM sensors are triaxial fluxgate magnetometers that are mounted on 0.5 m booms on the F15–F18 spacecraft. Magnetic vectors are sampled 12 times per second. One second average values are calculated as $dB = B_{meas} - B_{IGRF}$, the differences between measured and International Geomagnetic Reference Field (IGRF) values of magnetic fields at the spacecraft locations. Data are presented as dB_X, dB_Y, and dB_Z in spacecraft-centered coordinates. The X and Y axes point toward spacecraft nadir and along the velocity vector, respectively. The Z axis completes the right-hand system. Nearly simultaneous observations from the SSM and SSIES sensors on the various DMSP spacecraft help corroborate and interpret electrodynamic measurements in the storm's main phase. Velocity and magnetic field observations are combined to calculate Poynting flux, as described below.

In order to estimate the contribution to the energy budget due to particle precipitation, we use a modified Hemispheric Power (HP) by combining the NOAA HP with the DMSP HP. The HP was originally devised for the NOAA/TIROS satellites [*Evans*, 1987; *Fuller-Rowell and Evans*, 1987] and is a semiempirical model based on the precipitating energy flux carried by energetic electrons at latitudes poleward of 45°. The DMSP HP was adapted from the NOAA HP [*Emery et al*., 2008]. There are slight differences between the two HP indices. We use the average of the two for this paper, which we refer to as HP.

Neutral densities on the GRACE satellite were measured using superSTAR accelerometers, using the techniques of *Sutton et al*. [2005] and *Sutton* [2009]. These measurements are similar to those made by the STAR accelerometer on CHAMP [*Bruinsma et al*., 2004; *Sutton*, 2009], with a precision an order of magnitude greater than the CHAMP instrument. During the period of interest, the satellite is in a 451 × 481 km orbit, with inclination of 89° and average altitude of 470 km.

In this study we use the GRACE data in several ways, first as orbit averages in which a running mean of 5 s data is averaged over one orbit. We also show data along the orbit track, where all the values have been mapped to a constant altitude of 400 km by the Naval Research Laboratory Mass Spectrometer Incoherent Radar 2000 (NRL-MSISE00) [*Picone et al*., 2002] model. In this case, data are averaged in 3° wide latitude bins. Finally, a wave analysis using data from both GRACE A and GRACE B satellites has been carried out. This is described in more detail below.

Neutral wind observations during the storm were obtained from the Neutral Wind Meter (NWM) on board the Communication/Navigation Outage Forecast System (C/NOFS) satellite [*Earle et al*., 2013]. C/NOFS was in a

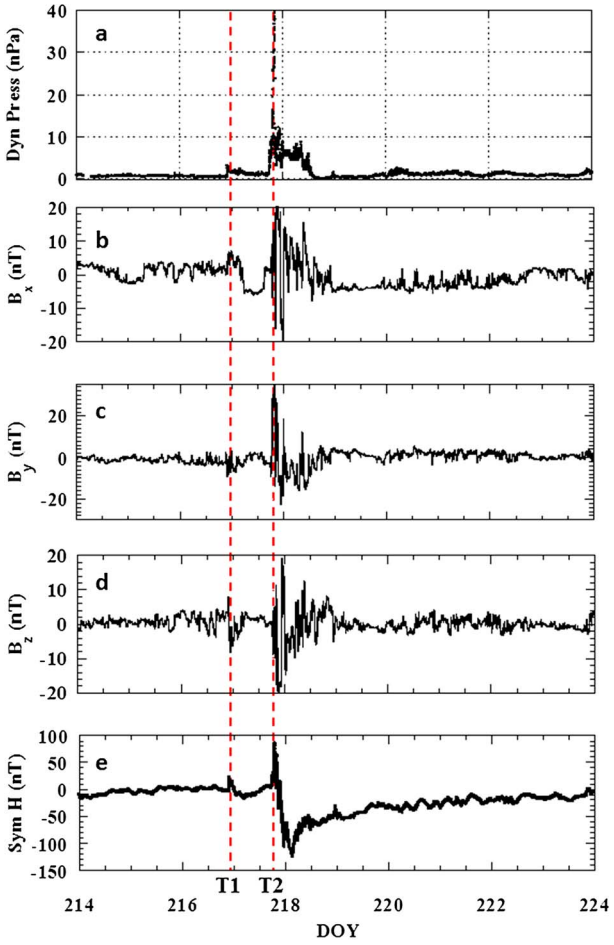

Figure 1. Solar wind observations and *Sym-H* index for the period 2–12 August 2011. (a) The solar wind dynamic pressure. (c–d) The three components of IMF in GSM coordinates are shown, followed by the (e) *Sym-H* index. Vertical dashed red lines labeled T1 and T2 correspond to times 21:59 UT on DOY 216, and 19:06 UT on DOY 217, respectively. At T1 there is a sharp increase in solar wind dynamic pressure, and storm onset occurs at T2.

13° inclination, 402 × 808 km orbit during the August 2011 storm. We use geographic coordinates to report NWM measurements as is common with neutral winds or densities which are usually not responsive to the magnetic field. Due to the low neutral densities measured at this time, only points near perigee at approximately 400 km altitude are employed in the analysis. This limits the data to one averaged point per orbital period of ~100 min. During the August magnetic storm, the perigee location is initially over the western edge of South America, 10°–12° south of the geographic equator, at approximately 17:30 LT on day of year (DOY) 217.5. On each subsequent orbit the perigee point moves by ~25° to the west, as the satellite perigee location moves from 17:30 to 18:10 LT over 2 days. Only cross-track data in the horizontal plane were available. Given the low-inclination orbit of C/NOFS, the cross-track neutral winds are roughly equal to the meridional winds during the storm main phase. At the start of the 5 August 2011 (DOY 217), the winds are set to zero. All the values reported in this paper are perturbations from that zero baseline.

3. Observations

3.1. Ionospheric Power Input

The solar wind dynamic pressure and Interplanetary Magnetic Field (IMF) (in GSM coordinates) values for 2–12 August 2011 are shown in Figure 1, together with the *Sym-H* index for the period. In Figure 1, vertical dashed lines labeled T1 and T2 indicate (1) a sharp increase in solar wind density and velocity leading to increased solar wind dynamic pressure; (2) the storm commencement identified by the sharp decrease in *Sym-H* index. These

times are 21:59 UT on day 216 (4 August) and 19:06 UT on day 217 (5 August), respectively. The solar conditions leading up to the main onset on 5 August are complicated. Three Coronal Mass Ejections (CMEs) were launched from the Sun on 2–3 August, reaching the Earth on 4–5 August. The small increase in dynamic pressure and *Sym-H* at T1 may be caused by arrival of a weak CME or may be a high-speed stream event. The system appears to relax to the previously quiet conditions over the following hours. The following two CMEs merge and cause the main storm at T2, marked by a sharp increase in dynamic pressure and large oscillations in IMF. A description and numerical simulation of solar wind conditions are provided by *Lee et al*. [2013].

The *Sym-H* index reaches a minimum of −126 nT at 0322 UT on 6 August. This is followed by an unusually slow recovery over several days, with *Sym-H* returning to zero on 13 August (day 225). During the extended recovery, solar wind dynamic pressure initially remains high and variable for some hours, and large variations in IMF persist through DOY 218. The two-step increase in solar wind dynamic pressure and power available to the IT system means that the storm effects which begin at 1906 UT are preceded by a smaller prestorm period in which energy is also available to the system. Additional variations in dynamic pressure during the first hours of the storm recovery also complicate the effects of the storm.

We estimate the Poynting flux from DMSP observations of cross-track velocities from the IDM, together with the measured values of dB made by the SSM and **B** from the International Reference Geomagnetic Field (IGRF), following the methodology outlined by *Huang and Burke* [2004]. As we disregard the in-track velocity component, the downward directed (S_X in the spacecraft-centered coordinate system) Poynting flux is estimated as

$$S_X = (1/\mu_0)[(V_X \cdot B_Z - V_Z \cdot B_X)dB_Z - (-V_X \cdot B_Y)dB_Y] \quad (1)$$

In addition to the DMSP observations, we employ the W05 empirical model for global predictions of Poynting flux across both hemispheres in order to expand the estimate of energy input across all local times. Input to W05 are the solar wind IMF, velocity, and density obtained from the OMNI website. The coordinates of the model and DMSP data are Altitude Adjusted Corrected Geomagnetic Coordinates. We use the default temporal resolution of the model which is 4 min, interpolating all input to match the model cadence. A comparison of the model and data are shown in Figure 2. In Figure 2 (top), red crosses are the Northern Hemisphere satellite track in corrected magnetic coordinates [*Hultqvist*, 1958a, 1958b] of DMSP F15 starting at 2212 UT, together with the contours of Poynting flux predicted by W05. The equatorward boundary of the oval defined by W05 as the region outside which the electric field is zero is shown by a black line. In Figure 2 (bottom), the values of the model (Figure 2, black) and data (Figure 2, red) are shown for the DMSP orbital track. In Figure 2, dotted vertical lines indicate the location of 45° MLat. The comparison between model and data indicates that the spatial distribution on any particular crossing is not predicted well by the model during this selected period.

We compare the path-integrated average Poynting flux for DMSP F15, 16, and 18 along the satellite track for days 216–222, with the predictions of W05 for the same locations (not shown). While the absolute values show some discrepancy with W05 consistently higher than the DMSP values, overall the agreement in temporal variation is remarkably good. For the rest of this paper, we use the integrated W05 predictions, scaled by the DMSP data, for global estimates of total Poynting flux during the storm. The scaling factor is obtained from the ratio between the predictions of W05 and the measured Poynting flux from DMSP. Scaling factors are estimated from the sum of the average integrated Poynting flux measured by F15, 16, and 18 in the Northern and Southern Hemispheres separately and for quiet and active periods during the entire interval. We compare these to W05 and the ratio (Poynting flux predicted by W05 along DMSP F15, 16, and 18 satellite tracks)/(sum of average Poynting flux measured by DMSP F15, 16, and 18) gives the scaling factors. We define the active period as the time between days 217.7 and 218.8. For this interval, the scaling factor in the Northern Hemisphere is 1.06 and in the Southern Hemisphere 1.26. Prior to and following this interval, the scaling factor is 3.05 in the Northern Hemisphere and 3.18 in the Southern Hemisphere. These factors indicate the level to which W05 overestimates the Poynting flux. Scaling the predictions of W05 down (hereafter referred to as $W05_{DMSP}$), we use $W05_{DMSP}$ to calculate the total Poynting flux input to the ionosphere during the storm. In Figure 3a we show the original W05, together with $W05_{DMSP}$ derived by this scaling procedure for comparison.

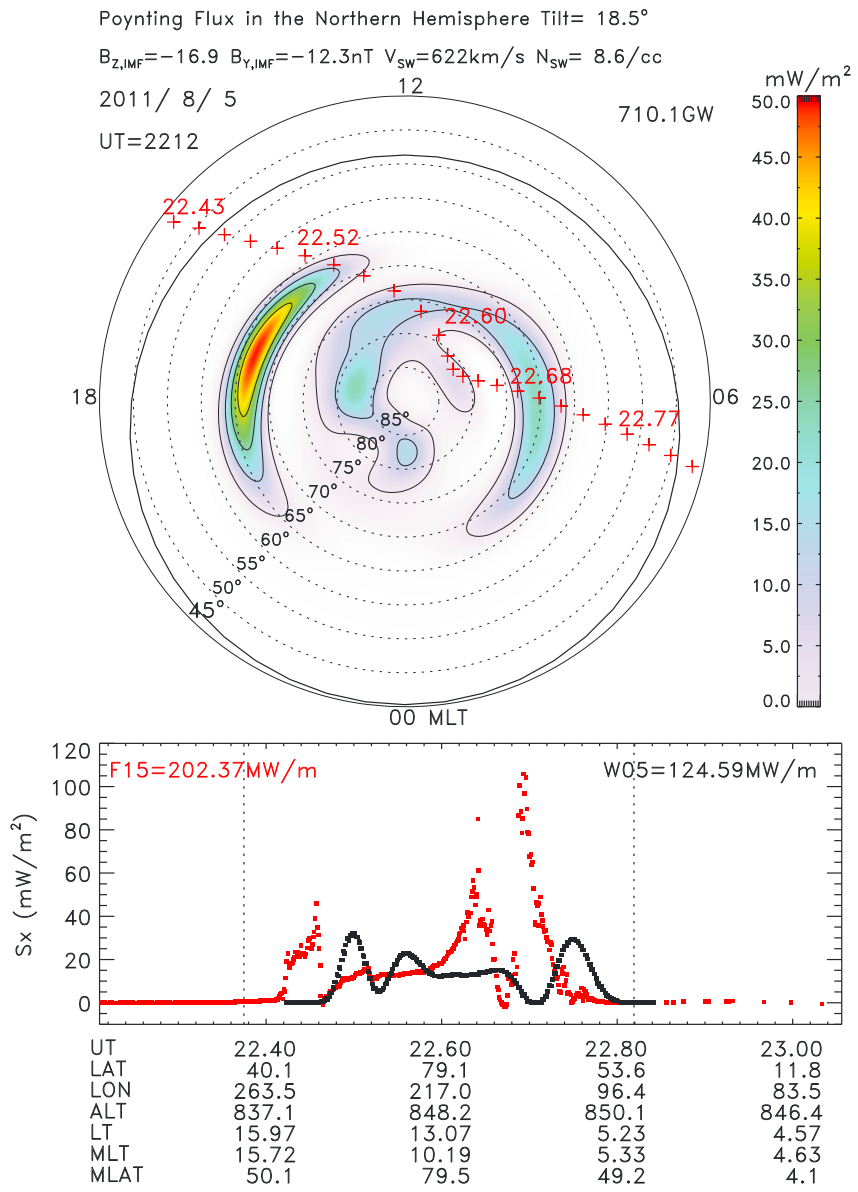

Figure 2. (top) DMSP F15 pass over the northern polar cap is shown, together with the W05 contours of Poynting flux, plotted in CGM coordinates. The time of the crossing begins at 22:12 UT on DOY 217. The red crosses indicate the DMSP trajectory with the UT times labeled in red. The black contour offset from the magnetic pole denotes the limit of the electric potential. (bottom) The measured values of S_X along the DMSP satellite track in red dots, together with the W05 predictions in black. Vertical dotted lines denote the limit of the electric potential, typically 45° MLat. Satellite ephemeris and UT are indicated at the bottom. The orbit-integrated values of Poynting flux for this pass are listed in the upper corners, with F15 value in red and W05 value in black.

The W05 model does not include the effect of particle precipitation. The NOAA and DMSP HP and the average of the two are shown in Figure 3b, for the storm period. We add the Hemispheric Power to the scaled Poynting flux predicted by $W05_{DMSP}$ to obtain the total power input ($W05_{adj}$ hereafter) to the ionosphere during the storm. The total power, $W05_{adj}$, is shown in Figure 3c. This total power is used to calculate Tc, the nighttime minimum of the global exospheric temperature distribution [*Jacchia*, 1970], and dTc, the adjustment of Tc to fit observed thermospheric densities. The value of dTc for the original W05 and the $W05_{adj}$ are shown in Figure 3d. The application of dTc obtained from $W05_{adj}$ is described below.

The ring current is also a sink for storm energy. We calculate this term using the Dessler-Parker-Sckopke relation [*Dessler and Parker*, 1959; *Sckopke*, 1966] which states that the ring current energy (J) can be written

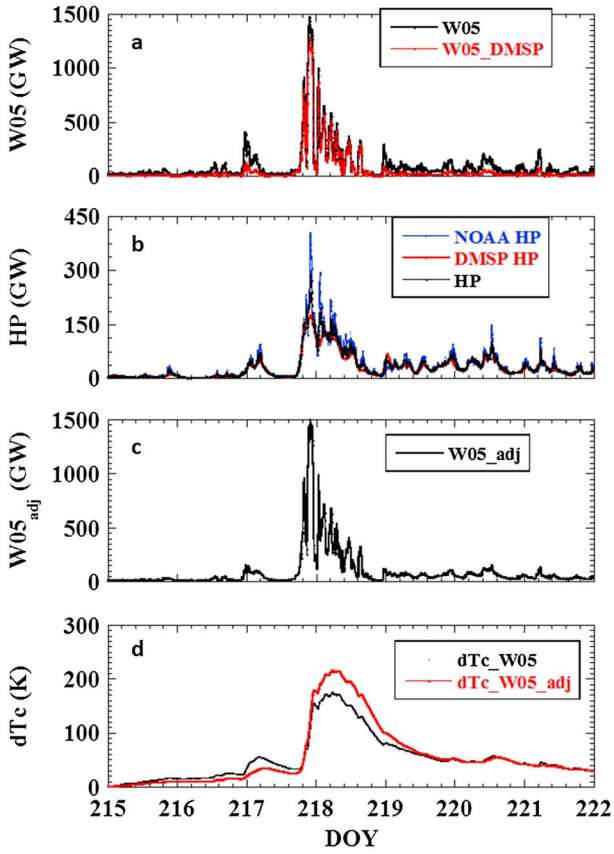

Figure 3. From top to bottom are shown (a) original W05 predictions of Poynting flux in black, $W05_{DMSP}$ shown in red; (b) NOAA HP (blue), DMSP HP (red), and the HP (= (NOAA HP + DMSP HP)/2) (black) used in this paper; (c) the final $W05_{adj}$ used in our study; (d) dTc from W05 (black) and adjusted dTc from $W05_{adj}$ (red) are shown for the period from 3 to 10 August 2011.

as $-3.85 \cdot 10^{13}$ *Dst* (nT). We use *Sym-H* which is a 1 min ring current index to illustrate the temporal variations not apparent in the 1 h *Dst* index.

3.2. Thermospheric Energies

We estimate the change in average total thermospheric energy during the storm due to Joule heating following the methodology outlined by *Burke et al.* [2009]. We set the lower boundary of the thermosphere at 100 km and integrate over the altitude range assuming that mass densities can be related to temperature as in the Jacchia series of empirical models. This model assumes that diffusive equilibrium holds during the entire interval, a reasonable assumption in our study since we are not concerned with rapid temporal variations. As the time intervals over which we estimate the energy are long (100 min for GRACE orbital period, 3 h for HASDM sampling), temporal variations small compared with the orbit duration of 100 min are averaged out. Neutral density and temperature are exponential functions of altitude in this model.

Our calculation is based on the Jacchia model and all Jacchia-type models such as Jacchia-Bowman 2008 and the extension of W05 to thermospheric densities and temperatures. A full description of the Jacchia model can be found in *Jacchia* [1970]. Briefly, all Jacchia-type models are parameterized by Tc, the nighttime minimum in the global exospheric temperature. Tc is a function of the $F_{10.7}$ index and mean $F_{10.7}$. The neutral temperature at any location is a function of the exospheric temperature which in turn is a function of time, latitude, longitude, Tc, and a_p. The neutral density is a function of the temperature profile at any height, and can be expressed

$$\frac{\mathrm{d}(\ln n_i)}{\mathrm{d}z} = -\frac{m_i g}{kT} - (1+\alpha_i)\frac{\mathrm{d}(\ln T)}{\mathrm{d}z} \tag{2}$$

where $i = (O, O_2, He, Ar, N_2)$; n = number density; m = molecular mass; g = gravitational acceleration, T = temperature, α = thermal diffusion coefficient = −0.38 for He and zero for all other ions. This equation

can be integrated numerically to specify all n_i at any height, once the temperature profile which is defined entirely by Tc, and lower boundary condition are given.

Once n_i is calculated, mass density is found by

$$\rho = \Sigma m_i n_i \tag{3}$$

Thus, by specifying Tc, the entire thermosphere—number density, mass density, and temperature at all locations—is determined.

The quantity dTc is the adjustment made to the Jacchia model to fit observations. Tc is replaced by (Tc + dTc). This has been done in many previous studies—see *Marcos et al*. [1998], *Storz et al*. [2005], *Wilson et al*. [2006], *Bowman et al*. [2008], *Burke et al*. [2009], *Weimer et al*. [2011], *Sutton et al*. [2012], and others.

Total energy input into the thermosphere during stormtime heating is due to (1) the increase in thermal energy and (2) the increase in gravitational energy as the thermosphere expands

$$E = H_T + \Phi_G \tag{4}$$

where H_T is the thermal energy in the thermosphere, and Φ_G is the work done against gravity.

$$H_T = \int_0^{2\pi}\int_0^{\pi}\sin\theta \int_{R_E+h_0}^{\infty} \eta_T(r,\theta,\varphi) r^2 \mathrm{d}r\, \mathrm{d}\theta\, \mathrm{d}\varphi \tag{5}$$

where η_T is the energy density in the thermosphere and is written

$$\eta_T(r,\theta,\varphi) = C_V(r,\theta,\varphi) n(r,\theta,\varphi) T(r,\theta,\varphi)/A \tag{6}$$

C_V, n, T, and A are the heat capacity, number density, temperature and Avogadro's number, respectively.

$$C_V(r,\theta,\varphi) \approx \frac{k_B A}{n(r)}\left\{\frac{5}{2}(n[\mathrm{N_2}] + n[\mathrm{O_2}]) + \frac{3}{2}(n[\mathrm{O}] + n[\mathrm{Ar}] + n[\mathrm{He}] + n[\mathrm{H}])\right\} \tag{7}$$

K_B is Boltzmann's constant, the neutral gas constituents N_2, O_2, O, Ar, He, and H are taken from the Jacchia model. The approximate symbol is used to account for chemical reactions not contained in the models.

The gravitational energy is written

$$\Phi_G = \int_0^{2\pi}\int_0^{\pi}\sin\theta \int_{R_E+h_0}^{\infty} \phi_G(r,\theta,\varphi) r^2 \mathrm{d}r\, \mathrm{d}\theta\, \mathrm{d}\varphi \tag{8}$$

where the gravitational potential is

$$\Phi_G(r,\theta,\varphi) = \rho(r,\theta,\varphi) M_E G\left(\frac{1}{r_0} - \frac{1}{r}\right) \tag{9}$$

ρ is the mass density in the thermosphere, M_E is the mass of the Earth, and G is the gravitational constant. We set the potential to zero at the lower limit of the height integration, set to 100 km. Because the thermal and gravitational energy densities are proportional to the exponentially decaying neutral density, little accuracy is lost by imposing a practical upper boundary of 1000 km.

For this study, we used Jacchia-Bowman 2008 (hereafter JB08) [*Bowman et al*., 2008] to compute the energy corresponding to the observed change in neutral density. JB08 gives a relationship between *Dst* and global neutral densities, parameterized by Tc. Given any value of density at a specific altitude and *Dst*, the densities and temperatures at all locations are predicted by the Jacchia-type model as described by equation (2). Equation (6) gives a one-to-one relation linking neutral density (n), temperature (T), and energy density (η). For each of the sources of neutral density, both from observations and empirical models (GRACE, HASDM, and $W05_{adj}$), we scale Tc in JB08 to fit the density measurement or model prediction. This gives dTc which is applicable to any model based on the Jacchia model. From this scaling we obtain a one-to-one relationship

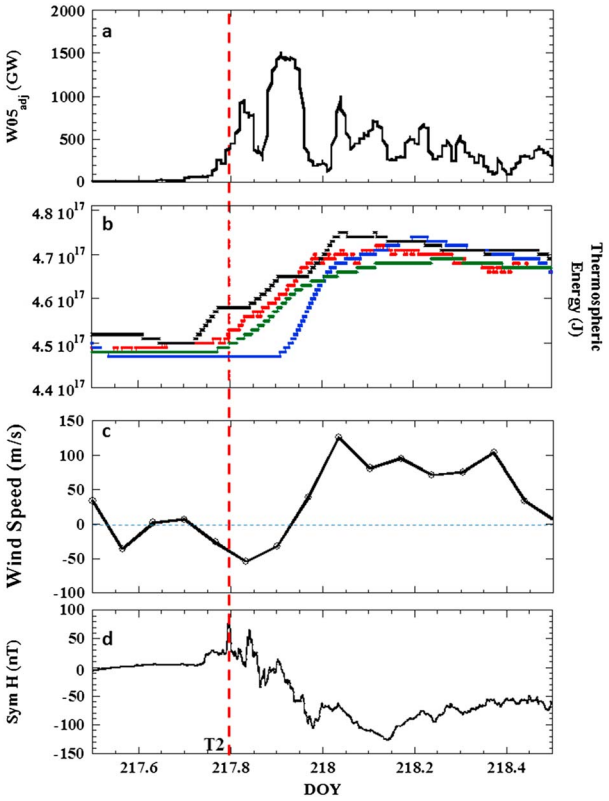

Figure 4. From top to bottom are shown (a) $W05_{adj}$ total Poynting flux; (b)thermospheric energy from GRACE (red), HASDM (black), $W05_{adj}$ (green), and Jacchia-Bowman 2008 (blue); (c) the meridional wind measured by NWM with dashed line indicating zero; (d) *Sym-H* index for day 217.5 to 218.5. The vertical dashed red line labeled T2 indicates the time of storm onset.

between measured neutral density and energy at any satellite location. The total energy is obtained by integration over space using the JB08 model for spatial variations. For all these calculations, the HASDM, W05, and JB08 models are sampled along the GRACE orbit. Finally, an orbit running mean is taken through all results to remove orbit-scale oscillations resulting in an orbit-averaged value of neutral energy with a cadence of 5 s. Note that as the temporal resolution of HASDM is 3 h, the effect of this procedure gives a more gradual temporal variation in energy than the original model.

3.3. IT Power, Energy, and Transport

Results of the estimates of ionospheric power (Poynting flux plus HP), thermospheric energy, and measured meridional wind and *Sym-H* are shown in Figure 4 for the time interval from UT day 217.5 to 218.5. Figure 4a shows the $W05_{adj}$ values of total power; Figure 4b shows the values of thermospheric energy calculated for HASDM (black), GRACE (red), W05 (green), and JB08 (blue). Note that the W05 model has been adjusted, with new dTc calculated to correspond to the scaled Poynting flux and HP as described above. Figure 4c shows the approximate meridional wind speed. In the coordinate system used to plot the winds, positive is northward which is equatorward at this time since C/NOFS is in the Southern Hemisphere. At Figures 4d is shown the *Sym-H* index. In Figure 4 the red dashed line, labeled T2 is the same time as that shown in Figure 1 and corresponds to 1906 UT on day 217, the onset of the magnetic storm.

It can be seen that the energy in the ionosphere starts to increase prior to the storm onset, possibly corresponding to the small increase in *Sym-H* prior to T1. As noted earlier, the solar wind response is complicated by multiple CME events or possibly a mix of high-speed stream and CMEs. There are multiple increases in $W05_{adj}$ during the period following storm onset, possibly also a response to the variations in solar wind dynamic pressure evident in Figure 1a. There are differences between the four sources of neutral energy shown in Figure 4b, one derived from direct measurement of neutral density (GRACE), a second derived from measurements of satellite drag (HASDM), the third and fourth obtained from empirical models (JB08 and $W05_{adj}$). It should be noted that HASDM has 3 h resolution, hence the apparent discontinuities in the plot. HASDM shows an increase before the other traces. GRACE and $W05_{adj}$ are in good agreement during the main phase and recovery, and JB08 shows the longest delay in thermospheric response to the storm. We ascribe the discrepancy between HASDM and GRACE observations to the limited local time coverage by GRACE during this time. HASDM, which is limited by 3 h resolution, has global coverage of all local times which may explain the faster response. For the rest of this paper, we will use the GRACE data to represent the thermospheric response, bearing in mind that the spatial coverage offered by the satellite may not fully capture global storm effects.

The meridional winds begin to turn equatorward at 217:23:14 UT, approximately 4 h after the storm commencement at 217:19:06 UT and 23.25 h from the solar wind compression at T1. The measured winds reach a maximum of 126 m s^{-1} at 218:00:50, approximately when the thermospheric energy also reaches a maximum, and remain strongly equatorward with a median wind speed of 78 m s^{-1} over the next 8 h, finally decreasing at 218:12:09 UT.

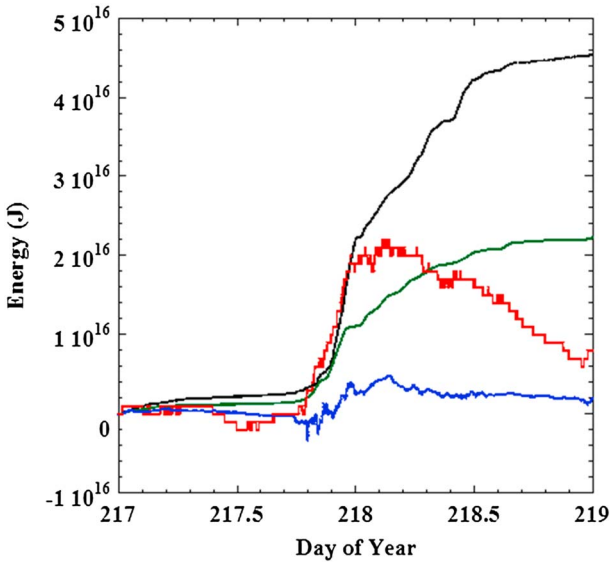

Figure 5. The computed energy into the MIT system is shown in black, the thermospheric energy increase in red, total ionospheric energy input in green, and ring current energy in blue. All values have been set to zero at the start of DOY 217.

Overall, the power input to the ionosphere tapers off faster than the thermospheric energy which remains high after the main phase of the storm has ended and recovery begins. As noted in Figure 1, the *Sym-H* (or *Dst*) index shows an unusually gradual recovery over several days.

3.4. Energy Input From the Solar Wind

To put our estimates into context, we calculate the energy available to the magnetosphere-ionosphere-thermosphere (MIT) system from the solar wind. We use the coupling parameter given by *Perreault and Akasofu* [1978] which is

$$U_\varepsilon = \frac{4\pi}{\mu_0} V_{SW} B_{SW}^2 \sin^4\left(\frac{\theta_c}{2}\right) l_0^2 \qquad (10)$$

where U_ε is the input power in Watts, μ_0 is the magnetic permeability of free space, B_{SW} is the magnitude of the IMF, θ_c is the IMF clock angle, and l_0 is the linear effective cross-sectional area of the solar wind-magnetosphere interaction. The empirically determined range of l_0 is 3.3 to 4.6 R_E [*Burke et al.*, 1999]. In this paper, we use a value of 4.6 R_E which gives us the most reasonable fit to the observed energy sinks.

In Figure 5 we show the results of the energy estimates, where total power into the system (equation (10)) and ionospheric power input ($W05_{adj}$) have been integrated from a starting time at the beginning of day 217. Thermospheric and ring current energy are set to zero at this same time. In black is shown the total energy available to the MIT system; the change in thermospheric energy observed by the GRACE satellite is plotted in red; the integrated total ionospheric energy $W05_{adj}$ is shown in green, and the change in ring current energy is plotted in blue.

For the first 3 h of the main phase of the storm, the thermosphere is the dominant sink for solar wind energy input. At this time it is approximately equal to the total ionospheric energy input from the sum of Poynting flux and particle precipitation. As we have noted above, the Poynting flux is derived from a semiempirical model modified by DMSP observations, as is the HP. We expect that both models are subject to error when used to forecast specific storm events. The thermospheric energy is similarly subject to error as we have assumed that the local orbit-averaged observations from GRACE can be extrapolated to all local times using a Jacchia-type model. However, the point of Figure 5 is that the thermosphere is a large sink for stormtime energy input, comparable with the ionosphere.

4. Discussion

Cusp upwelling of the thermosphere has been shown for the CHAMP satellite [*Lühr et al.*, 2004] where density structures accompanied by small-scale field-aligned current (FAC) filaments were observed under all levels of magnetic activity. Stormtime increases in neutral density were reported by *Liu et al.* [2010]. In this latter study which included all magnetic storms which occurred between 2002 and 2005, 90% of the storms showed density increases within 10° of the magnetic pole. Events in which large density enhancements occurred in the cusp during events characterized by large IMF B_y have been modeled by *Crowley et al.* [2010]. Near-simultaneous increases in Poynting flux and neutral densities occurring at very high latitudes during solar wind pressure pulse events were reported by *Shi et al.* [2012]. This is confirmed in our analysis of the August 2011 magnetic storm (not shown). A detailed study of the 6 November 2001 storm by *Mishin et al.* [2007] shows similar phenomena as reported in this paper—prompt high-latitude thermospheric response at the start of the storm accompanied by enhanced electric fields.

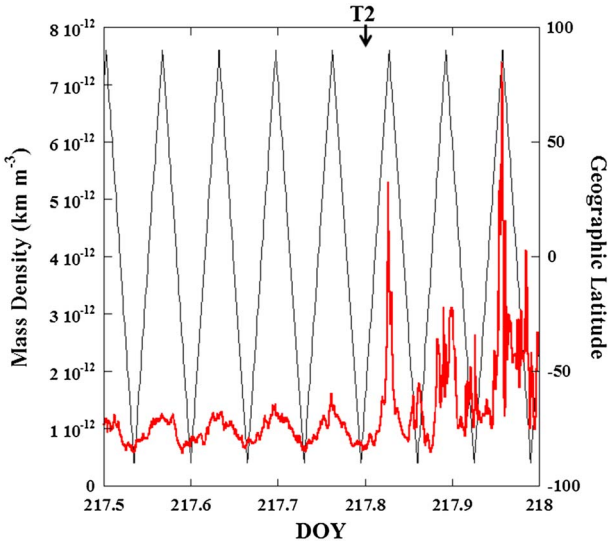

Figure 6. GRACE mass densities and orbit geographic latitudes are shown as functions of DOY for the interval DOY 217.5 to 218, in which the storm onset time at T2 is indicated by the black arrow above the plot. Sharp increases in density are clear at polar latitudes over the three orbits from DOY 217.76 which precedes the storm onset, to the peak density at 217.96.

During the August storm, we saw similar intense spikes of neutral density in GRACE data. Figure 6 illustrates the mass density observed by GRACE during the interval from DOY 217.5 to 218, together with the geographic latitude of the satellite track. Storm onset occurs at DOY 217.8 which is indicated by the arrow labeled T2. As we have pointed out above, there is a dynamic pressure enhancement which occurs at 21:59 UT on day 216, to which there is a thermospheric response. The response to the storm onset at T2 is apparent at high latitudes over three full orbits beginning just before T2. A large localized increase in density occurs on the first high-latitude crossing after T2. The Northern Hemisphere shows a much larger response, but there are also clear density enhancements in the Southern Hemisphere. The same hemispheric asymmetry in thermospheric response to solar wind driving was noted in the study by *Liu et al*. [2010] which showed a larger number of events in the northern polar cap regardless of season. Of note in Figure 6 is that virtually all the density maxima during these three orbits occur at the highest geographic latitudes reached by the satellite. As we will show below, there is evidence of Traveling Atmospheric Disturbances (TADs) indicative of Joule heating at very high latitudes at 22 LT at approximately DOY 217.96.

Poynting flux in the high-latitude regions has also been reported by *Knipp et al*. [2011]; *Wilder et al*. [2012] and modeled by *Li et al*. [2011]. In these studies, the emphasis has been on the cusp as the region where sharply localized intense Poynting flux and neutral density enhancements occur, but they also show that higher Poynting flux extends across flow channels in the polar cap. It should be noted that the lack of particle observations on F15 makes it impossible to characterize the particle deposition regions for this spacecraft. It is possible that due to orbital coverage, the cusp is infrequently encountered, and the resulting DMSP integrated Poynting flux which we use to scale W05 is underestimated. However, there are clearly regions at very high latitudes in which enhancements in Poynting flux are detected by DMSP. An example of a high-latitude crossing in which this occurs is illustrated in Figure 2 (bottom). Poynting flux measured by DMSP F15 shows a large enhancement at latitudes poleward of both dawn and dusk auroral zones. The peak value of 85.16 MW m^{-2} is detected at 22:38.5 UT, at magnetic latitude of 83.1°N and 9.6 MLT. While this is a likely location for the cusp, the shape of the integrated Poynting flux curve in Figure 2 indicates that there is a broad area of high Poynting flux at high latitudes, combined with a narrow region of intense Poynting flux. This observation supports reports of high-latitude flow channels in the polar cap associated with reconnection. Several DMSP passes show a broad region in which Poynting flux enters the ionosphere at very high latitudes. Note that for this particular event, W05 does not predict the magnitude or distribution of Poynting flux in the polar cap well as can be seen in Figure 2 (bottom). In this pass, as in most of the DMSP passes during the storm, the highest Poynting fluxes predicted by W05 occur at auroral latitudes which are also where the HP maximizes.

The relation between Poynting flux and thermospheric heating is complex, since the interaction is mediated by ions. Briefly, the general hypothesis is that ions are energized by Poynting flux. The ions interact with neutrals in two ways, by collisions or by friction, the particular interaction dependant on the relative densities of both species. This leads to Joule heating of neutrals. If this hypothesis is correct, thermospheric heating during storms must be preceded by increased Poynting flux. The outstanding question in our study is where this occurs, at auroral latitudes or the polar cap. We attempt to address this question by considering (1) the energy balance for the storm and (2) timing of the observation of thermospheric energization relative to ionospheric energization.

Figure 5 shows the available source and three sinks for solar wind energy during the storm. Note that the ionospheric sink predicted by $W05_{adj}$ is dominated by Poynting flux and particle precipitation in the auroral zone. The ionospheric sink is approximately the same magnitude as the thermosphere, but the conventional view that energy is transferred from the auroral ionosphere to the thermosphere would imply that *all* energy reaching the ionosphere (Figure 5, green line) is transferred to the thermosphere (Figure 5, red line) since these two quantities are approximately equal at the start of the storm main phase. This cannot be true, since the ionosphere clearly shows the effects of strong energy input in the form of particle heating and field-aligned currents. This implies that significantly more energy must enter the ionosphere than is transferred to the thermospheric sink. Our conclusion is that the thermosphere cannot be heated via transfer of energy from the auroral ionosphere alone—the observed magnitude of the increase in thermospheric energy rules out this possibility. The only other location where energy is available to energize the thermosphere is the high-latitude region, i.e., the polar cap, which is not well represented by W05 (D. R. Weimer, personal communication, 2013). We conclude that a substantial amount of energy enters the IT system at very high latitudes, and this is not fully captured by $W05_{adj}$.

Further, the response of the neutrals which appears almost simultaneous with the increase in Poynting flux or particle precipitation energy at the start of the storm main phase is problematic. The same fast response has been reported in other studies [*Mishin et al*., 2007]. The timing of the increase in the integrated global thermospheric energy rules out the possibility that energy is dissipated first in the auroral ionosphere, then transitioned to the thermosphere via collisional or frictional heating [*Vasyliunas and Song*, 2005], a process which is expected to take 3–6 h, according to numerical simulations of the IT system [*Huang et al*., 2012]. The dilemma raised by both the timing of the appearance of heated neutrals, and the magnitude of the required energy, may be explained as underestimation of Poynting flux within the polar cap. This is true of both DMSP observations and the W05 model. Occasional appearance of very intense spikes of Poynting flux at DMSP locations suggests that the cusp is a major area for energy deposition, as has already been suggested [*Knipp et al*., 2011; *Li et al*., 2011]. Unfortunately, direct crossings of the cusp by DMSP are at best sporadic given the orbit. In addition to the cusp, occasional broad areas of elevated Poynting flux observed by DMSP within the polar cap indicate that the high-latitude regions are reservoirs for large amounts of electromagnetic energy [*Wilder et al*., 2012; *Eriksson and Rastatter*, 2013]. These areas are only occasionally encountered by DMSP. By contrast, the auroral ionosphere is crossed on every DMSP orbit, which leads us to believe that the auroral ionosphere is well represented both in our measurements of Poynting flux and the $W05_{adj}$ used in Figure 5. We suggest that contributions to total energy available to the IT system in the polar cap are not adequately measured or modeled; and hence, the conventional energy budget shown in Figure 5 may be seriously in error. To test our hypothesis, we examine direct responses of the thermosphere within the polar cap during the storm main phase. As already shown in Figure 6, spikes in neutral density occur at the highest latitudes reached by GRACE during the first 3 h of the storm.

In Figure 7 we show wave activity in the neutral mass density based on analysis of the density residuals from the GRACE satellite. Note that in this figure, all latitudes are geographic unless otherwise indicated. Figure 7a shows the residuals defined as the ratios of the density measured during the storm to the quiet time values on the preceding day during the ascending portion of orbits for preonset times (day 216, 00:53 UT to day 217, 19:05 UT) in blue and postonset times (day 217, 19:05 to day 218, 22:27 UT) in red. Figure 7b shows the density ratio for quiet-time values during the ascending portion of the satellite orbits. The color bar for the ratios is shown in Figure 7b (right), and the heavy black line is the *Kp* index during the storm. The *Kp* scale (unlabeled) is at the right of Figure 7b, ranging from 0 to 8, in increments of 1 *Kp* unit per tick. The maximum *Kp* during this storm was 7.7. The quiet-time densities used here are latitude-dependent values calculated from the mean density during day 216, well before the onset of the storm. Strong wave activity can be identified starting around 19:00 UT on day 217 and continuing for approximately 24 h.

Data from the two GRACE satellites, separated along their orbit by approximately 25 s, can be used to infer information on propagation characteristics of these Traveling Atmospheric Disturbances (TADs). When passing a peak or trough of TAD in quick succession, it is possible to establish the direction and speed of propagation in the satellite orbital plane. In most cases, this allows us to say whether a TAD is traveling poleward versus equatorward while giving an upper boundary for the propagation speed. The actual wave speed could be smaller if our assumed geometry for the angle between wave propagation and GRACE orbit is incorrect. Figure 7c shows TADs in mass density measurements from both satellites around 22:57 UT on day 217, at high northern geographic latitudes. Magnetic latitudes corresponding to the geographic latitudes

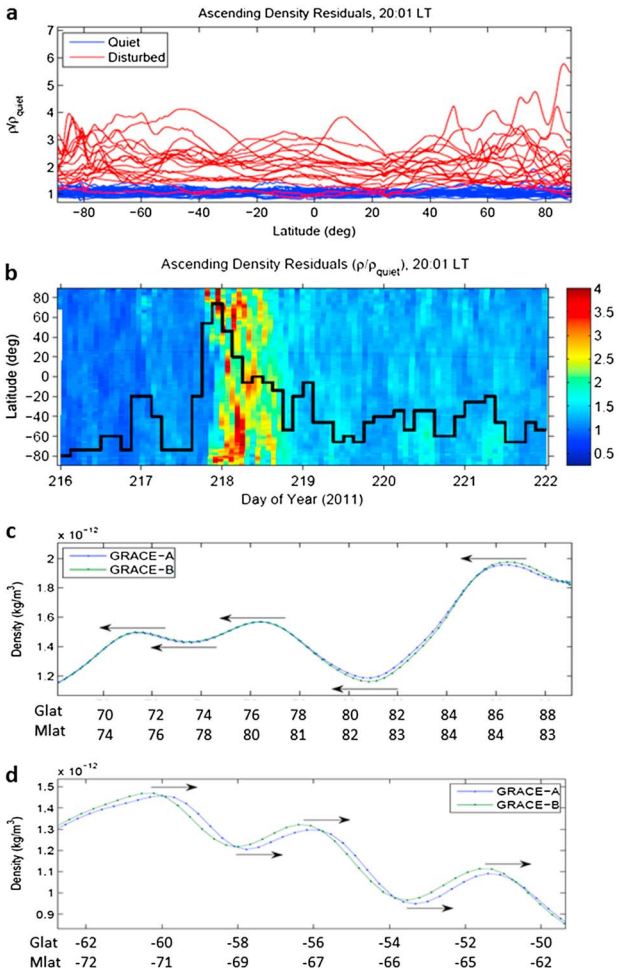

Figure 7. Waves in neutral density residuals, ρ/ρ_{quiet} from GRACE observations. From top to bottom are shown (a) wave activity at 20:01 LT from day 216 (blue) preceding the disturbed day and day 217 (red) which includes the start of the storm; (b) latitude dependence of the density residuals at 20:02 LT for days 216 to 222. The color bar at right shows the range of density ratios. The heavy line shows the *Kp* index during the storm. The *Kp* scale (unlabeled) is at right, ranging from 0 to 8, in increments of 1 *Kp* unit per tick; (c) TADs in the Northern Hemisphere, with arrows indicating the direction of propagation, and (d) TADs in the Southern Hemisphere, with arrows indicting the direction of propagation.

along the orbit are listed below the geographic latitudes in Figures 7c and 7d .The slight separation indicates an equatorward propagation with a maximum velocity of 200–300 m/s for the TADs equatorward of 8°N geographic latitude (GLat) and 500 m/s for the TAD near 86°N GLat. Figure 7d shows similar structures in the Southern Hemisphere, also traveling equatorward around 02:45 UT on day 218. The increased separation indicates a maximum propagation velocity of 800–1800 m/s. These large values may be indicative that the angle between TAD propagation and satellites' orbital plane is large. Note that the vertical scales in Figures 7c and 7d are different, with a higher maximum in Figure 7c.

Figure 7 shows that the waves with the largest amplitudes originate at very high latitudes, most clearly in the Northern Hemisphere. TADs are generally assumed to be gravity waves propagating away from a region in which Joule heating occurs [*Richmond*, 1978; *Balthazor et al*., 1997]. In our study, we use the TADs as a marker of the source region in which the neutrals are Joule heated. In Figure 7c, that source appears to be poleward of 83°N magnetic latitude (MLat); in Figure 7d, the source is poleward of −72°S MLat. While the figures are snapshots during the storm selected because the waves were particularly strong at these times, we assert that in the Northern Hemisphere, Joule heating must occur in the geographic polar cap, close to the magnetic pole and poleward of the auroral zone. In the Southern Hemisphere, the source is poleward of −72° which may be poleward of the auroral zone at this time. The wave analysis agrees with the appearance of neutral density spikes at the geographic poles shown in Figure 6.

The observations made by NWM located at −10° to −12°S geographic latitude show strong equatorward winds which persist from the start of DOY 218 until 12:09 UT on this day. The first appearance of equatorward meridional winds is approximately 4 h after the commencement of the storm. This timing alone rules out the possibility that winds originate near the poles since at the maximum observed magnitude of 126 m s^{-1}, it would take approximately 20 h for neutrals to move from the pole to the equator at C/NOFS location. Further, we would not expect the stormtime winds generated to dominate the normal wind pattern generated by the Earth's rotation.

However, the TAD velocities which are in the range of 800–1800 m s^{-1} in the Southern Hemisphere are in rough agreement with the 4 h delay. In numerical simulations of the thermospheric response during storms, TADs attenuate as they propagate away from the Joule heating source at high latitudes. They contribute to Joule heating of the thermosphere at lower latitudes via wave-neutral interactions [*Richmond*, 1978] and give rise to meridional winds [*Balthazor and Moffett*, 1999; *Gardner and Schunk*, 2010] in the range of ~ 100 m s^{-1}. This hypothesis appears to be confirmed by the NWM measurements, but further investigation is beyond this scope of this paper.

5. Summary and Conclusions

We have presented a coordinated set of observations of ionospheric and thermospheric responses to a moderate magnetic storm which occurred on 5–6 August 2011. By combining the DMSP observations of Poynting flux and particle precipitation with empirical models, we obtain the total energy deposited in the IT system. We computed the energy required to heat the neutral densities observed by the GRACE accelerometer. Comparing the energy input from the solar wind with the energy sinks in the form of Poynting flux, particle precipitation, ring current, and thermospheric heating, we conclude that the main source of thermospheric energy is not included in models of Poynting flux or particle precipitation. We suggest that the thermosphere is primarily energized at polar latitudes. We also postulate that the thermospheric response is remarkably fast, commencing with the sharp increase in solar wind dynamic pressure, when small localized increases in neutral density are observed, as reported by *Shi et al*. [2012].

Our suggestion that the polar cap region is the primary source of thermospheric heating is substantiated by the GRACE observations of neutral density spikes which are localized to very high latitudes during the first 3 h of the storm. In addition, wave analysis shows that TADs propagate from high latitudes toward the equator in both hemispheres. The source of Joule heating is poleward of 83° and 72° MLat in the Northern and Southern Hemispheres, respectively.

While previous studies have noted that sharp increases in both Poynting flux and neutral densities can occur at cusp latitudes, this study is the first to point out the necessity of a polar cap as a primary source of thermospheric heating. The nature of IT coupling that occurs within the polar cap in order to account for the change in thermospheric energy has been identified for specific cases [*Crowley et al*., 2010; *Li et al*., 2012; *Mishin et al*., 2007], but a general investigation which can replicate the global thermospheric energy response during storms has yet to be carried out. We intend to pursue this in future studies of IT coupling.

Acknowledgments
The authors thank D.M. Ober, G.R. Wilson, M.R. Hairston, and G.D. Earle for supplying us with DMSP and C/NOFS data used in this study. This research was supported by the Air Force Office of Scientific Research Laboratory Task LRIR 12RV10COR.

Robert Lysak thanks Mike Kosch and an anonymous reviewer for their assistance in evaluating this paper.

References

Akasofu, S.-I. (1981), Energy coupling between the solar wind and the magnetosphere, *Space Sci. Rev.*, *28*, 121–190.

Balthazor, R. L., and R. J. Moffett (1999), Morphology of large-scale traveling atmospheric disturbances in the polar thermosphere, *J. Geophys. Res.*, *104*(A1), 15–24.

Balthazor, R. L., R. J. Moffett, and G. H. Millward (1997), A study of the Joule and Lorentz inputs in the production of atmospheric gravity waves in the upper thermosphere, *Ann. Geophys.*, *15*, 779.

Bowman, B. R., W. K. Tobiska, F. A. Marcos, C. Y. Huang, C. S. Lin, and W. J. Burke (2008), A new empirical thermospheric density model JB2008 using new solar and geomagnetic indices, AIAA 2008 6438, *AIAA/AAS Astrodynamics Specialist Conference*, Honolulu, Hawaii, 18–21 August, 2008.

Bruinsma, S., D. Tamagnan, and R. Biancale (2004), Atmospheric densities derived from CHAMP/STAR accelerometer observations, *Planet. Space Sci.*, *52*, 297–312, doi:10.1016/j.pss.2003.11.004.2008.

Burke, W. J., D. R. Weimer, and N. C. Maynard (1999), Geoeffective interplanetary scale sizes derived from regression analysis of polar cap potentials, *J. Geophys. Res.*, *104*(A5), 9989–9994.

Burke, W. J., C. S. Lin, M. P. Hagan, C. Y. Huang, D. R. Weimer, J. O. Wise, L. C. Gentile, and F. A. Marcos (2009), Storm time global thermosphere: A driven-dissipative thermodynamic system, *J. Geophys. Res.*, *114*, A06306, doi:10.1029/2008JA013848.

Casali, S., and W. Barker (2002), Dynamic Calibration Atmosphere (DCA) for the High Accuracy Satellite Drag Model (HASDM), AIAA-2002-4888, *AIAA/AAS Astrodynamics Specialist Conference and Exhibit*, Monterey, California, Aug. 5–8, 2002.

Crowley, G. D. J., K. A. Knipp, J. Drake, E. S. Lei, and H. Lühr (2010), Thermospheric density enhancements in the dayside cusp region during strong B_Y conditions, *Geophys. Res. Lett.*, *37*, L07110, doi:10.1029/2009GLo42143.

Dessler, A. J., and E. N. Parker (1959), Hydromagnetic theory of magnetic storms, *J. Geophys. Res.*, *64*, 2239–2259.
Earle, G. D., R. L. Davidson, R. A. Heelis, W. R. Coley, D. R. Weimer, J. J. Makela, D. J. Fisher, A. J. Gerrard, and J. Meriwether (2013), Low latitude thermospheric responses to magnetic storms, *J. Geophys. Res. Space Physics*, *118*, 3866–3876, doi:10.1002/jgra.50212.
Emery, B. A., V. Coumans, D. S. Evans, G. A. Germany, M. S. Greer, E. Holeman, K. Kadinsky-Cade, F. J. Rich, and W. Xu (2008), Seasonal, Kp, solar wind, and solar flux variations in long-term single-pass satellite estimates of electron and ion auroral hemispheric power, *J. Geophys. Res.*, *113*, A06311, doi:10.1029/2007JA012866.
Eriksson, S., and L. Rastatter (2013), Alfvén Mach number and IMF clock angle dependencies of sunward flow channels in the magnetosphere, *Geophys. Res. Lett.*, *40*, 1257–1262, doi:10.1002/grl.50307.
Evans, D. S. (1987), Global statistical patterns of auroral phenomena, in *Proceedings of the Symposium on Quantitative Modeling of Magnetospheric-Ionospheric Coupling Processes*, pp. 325, Kyoto, Japan.
Fuller-Rowell, T. J., and D. S. Evans (1987), Height-integrated Pedersen and Hall conductivity patterns inferred from the TIROS-NOAA satellite data, *J. Geophys. Res.*, *92*(A7), 7606–7618.
Gardner, L. C., and R. W. Schunk (2010), Generation of traveling atmospheric disturbances during pulsating geomagnetic storms, *J. Geophys. Res.*, *115*, A08314, doi:10.1029/2009JA015129.
Huang, C. Y., and W. J. Burke (2004), Transient sheets of field-aligned current observed by DMSP during the main phase of a magnetic superstorm, *J. Geophys. Res.*, *109*, A06303, doi:10.1029/2003JA010067.
Huang, Y., A. D. Richmond, Y. Deng, and R. Roble (2012), Height distribution of Joule heating and its influence on the thermosphere, *J. Geophys. Res.*, *117*, A08334, doi:10.1029/2012JA017885.
Hultqvist, B. (1958a), The spherical harmonic development of the geomagnetic field, epoch 1945, transformed into rectangular geomagnetic coordinate systems, *Ark. Geophys.*, *3*, 53–61.
Hultqvist, B. (1958b), The geomagnetic field lines in higher approximation, *Ark. Geophys.*, *3*, 63.
Jacchia, L. G. (1970), New static models for the thermosphere and exosphere with empirical temperature profiles, *SAO Special Report No. 313*, Cambridge, MA, Smithsonian Institution Astrophysical Observatory.
Knipp, D., et al. (1998), An overview of the early November 1993 geomagnetic storm, *J. Geophys. Res.*, *103*, 26,197–26,220.
Knipp, D., S. Eriksson, L. Kilcommons, G. Crowley, J. Lei, M. Hairston, and K. Drake (2011), Extreme Poynting flux in the dayside thermosphere: Examples and statistics, *Geophys. Res. Lett.*, *38*, L16102, doi:10.1029/1022GL048302.
Knipp, D. L., L. Kilcommons, M. Hunt, V. Mlynczak, B. Pilipenko, Y. D. Bowman, and K. Drake (2013), Thermospheric damping response to sheath-enhanced geospace storms, *Geophys. Res. Lett.*, *40*, 1263–1267, doi:10.1002/grl.50197.
Lee, C., C. N. Arge, D. Odstrcil, G. Millward, and V. Pizzo (2013), Ensemble modeling of successive halo CME's observed during 2–4 2011, in *Solar Wind 13*, AIP Conf. Series, vol. 1539, pp. 223–226, American Institute of Physics, Melville, NY.
Li, W., D. Knipp, J. Lei, and J. Raeder (2011), The relation between dayside local Poynting flux enhancement and cusp reconnection, *J. Geophys. Res.*, *116*, A08301, doi:10.1029/2011JA016566.
Li, H., C. Wang, W. U. Xu, and J. R. Kan (2012), Characteristics of magnetospheric energetics during geomagnetic storms, *J. Geophys. Res.*, *117*, A01225, doi:10.1029/2012JA017584.
Liu, R., H. Lühr, and S.-Y. Ma (2010), Storm-time related mass density anomalies in the polar cap as observed by CHAMP, *Ann. Geophys.*, *28*(1), 165–180.
Lühr, H., M. Rother, W. Ko¨hler, P. Ritter, and L. Grunwaldt (2004), Thermospheic up-welling in the cusp region: Evidence from CHAMP observations, *Geophys. Res. Lett.*, *31*, L06805, doi:10.1029/2003GL019314.
Marcos, F. A., M. J. Kendra, J. M. Griffin, J. N. Bass, D. R. Larson, and J. J. Liu (1998), Precision low Earth orbit determination using atmospheric density calibration, *J. Astronaut. Sci.*, *46*(4), 395–409.
Mishin, E. G., F. A. Marcos, W. J. Burke, D. L. Cooke, C. Roth, and V. P. Petrov (2007), Prompt thermospheric response to the 6 November 2001 magnetic storm, *J. Geophys. Res.*, *112*, A05313, doi:10.1029/2006JA011783.
Perreault, P., and S. I. Akasofu (1978), A study of geomagnetic storms, *Geophys. J. R. Astron. Soc.*, *54*, 537–573.
Picone, J. M., A. E. Hedin, D. P. Drob, and A. C. Aikin (2002), NRL-MSISE-00 empirical model of the atmosphere: Statistical comparisons and scientific issues, *J. Geophys. Res.*, *107*(A12), 1468, doi:10.1029/2002JA009430.
Rich, F. J., and M. Hairston (1994), Large-scale convection patterns observed by DMSP, *J. Geophys. Res.*, *99*, 3827–3844.
Richmond, A. D. (1978), Gravity wave generation, propagation, and dissipation in the thermosphere, *J. Geophys. Res.*, *83*, 4131–4145.
Sckopke, N. (1966), A general relation between the energy of trapped particles and the disturbance field near the Earth, *J. Geophys. Res.*, *71*, 3125–3130.
Shi, Y., E. Zesta, H. Connor, E. K. Sutton, J. O. Wise, Y. Su, and S. H. Delay (2012), Effect of solar wind dynamic pressure enhancements on thermosphere neutral density, SA33A-2172, *AGU Fall Meeting*, *San Francisco*, *California*, December 2012.
Storz, M. F., B. R. Bowman, and J. I. Branson (2002), Dynamic calibration atmosphere (DCA) for the High Accuracy Satellite Drag Model (HASDM), AIAA-2002-4886, *AIAA/AAS Astrodynamics Specialist Conference and Exhibit*, Monterey, California, Aug. 5–8, 2002.
Storz, M. F., B. R. Bowman, M. J. I. Branson, S. J. Casali, and W. K. Tobiska (2005), High Accuracy Satellite Drag Model (HASDM), *Adv. Space Res.*, *36*, 2497–2505, doi:10.1016/j.asr.2004.02.020.
Sutton, E. K. (2009), Normalized force coefficients for satellites with elongated shapes, *J. Spacecr. Rockets*, *46*(1), 112–116, doi:10.2514/1.40940.
Sutton, E. K., J. M. Forbes, and R. S. Nerem (2005), Global thermospheric neutral density and wind response to the severe 2003 geomagnetic storms from CHAMP accelerometer data, *J. Geophys. Res.*, *110*, A09S40, doi:10.1029/2004JA010985.
Sutton, E. K., S. B. Cable, C. S. Lin, L. Qian, and D. R. Weimer (2012), Thermospheric basis functions for improved dynamic calibration of semi-empirical models, *Space Weather*, *10*, S10001, doi:10.1029/2012SW000827.
Vasyliunas, V. M., and P. Song (2005), Meaning of ionospheric Joule heating, *J. Geophys. Res.*, *110*, A02301, doi:10.1029/2004JA010615.
Weimer, D. R. (2005), Improved ionospheric electrodynamic models and application to calculating Joule heating rates, *J. Geophys. Res.*, *110*, A05306, doi:10.1029/2005JA010884.
Weimer, D. R., B. R. Bowman, E. K. Sutton, and W. K. Tobiska (2011), Predicting global average thermospheric temperature changes resulting from auroral heating, *J. Geophys. Res.*, *116*, A01312, doi:10.1029/2010JA015685.
Weiss, L. A., P. H. Reiff, J. J. Moses, R. A. Heelis, and D. B. Moore (1992), Energy dissipation in substorms, *Substorms I*, ESA SP-335, pp. 309-317, Eur. Space Agency, Paris.
Wilder, F. D., G. Crowley, S. Eriksson, P. T. Newell, and M. R. Hairston (2012), Ionospheric Joule heating, fast flow channels, and magnetic field line topology for IMF By-dominant conditions: Observations and comparisons with predicted reconnection jet speeds, *J. Geophys. Res.*, *117*, A11311, doi:10.1029/2012JA017914.
Wilson, G. R., D. R. Weimer, J. O. Wise, and F. A. Marcos (2006), Response of the thermosphere to Joule heating, *J. Geophys. Res.*, *111*, A10314, doi:10.1029/2006JA011274.

DISTRIBUTION LIST

DTIC/OCP
8725 John J. Kingman Rd, Suite 0944
Ft Belvoir, VA 22060-6218 1 cy

AFRL/RVIL
Kirtland AFB, NM 87117-5776 2 cys

Official Record Copy
AFRL/RVBXP/Dr. Cheryl Huang 1 cy

This page is intentionally left blank.